Direct numerical simulation study of droplet spreading on spherical particles

Powder Technology 354 (2019) 11–18

Contents lists available at ScienceDirect

Powder Technology

journal homepage: www.elsevier.com/locate/powtec

Direct numerical simulation study of droplet spreading on spherical particles

E. Milacic, M.W. Baltussen *, J.A.M. Kuipers

Multiphase Reactors Group, Department of Chemical Engineering and Chemistry, Eindhoven University of Technology, Postbus, 5600, MB, Eindhoven, the Netherlands

ARTICLE INFO

Article history:
Received 16 November 2018
Received in revised form 19 March 2019
Accepted 24 May 2019
Available online 28 May 2019

Keywords:
DNS
VOF-IBM
Drop
Particles
Hydrodynamics
Curvature

ABSTRACT

Direct Numerical Simulations have been performed to study the droplet spreading behaviour on a spherical surface. A coupled immersed boundary and volume of fluid method is used to represent the gas-liquid-solid interactions. The contact area of the droplet on the surface is recorded in order to fit the initial spreading with a power-law representation, using the contact-angle and interface curvature as fitting parameters. Small viscous droplets are used to reduce interfacial oscillations as well as low drop velocities to reduce impact forces. A decrease of spreading area with increasing curvature is observed. Moreover, the model shows good agreement compared to equilibrium states. A strong contact-angle dependence is found for the prefactor of the power law, which is expected, and a linear decrease was found in the exponent for increasing curvature of the surface.

1. Introduction

Fundamental understanding of droplet-solid interactions is relevant for many industrial processes, from spray coating to condensed mode polymerization. In these processes, the liquid is used for species deposition but also for effective heat removal. To determine the efficiency of these processes, proper droplet spreading is essential. For example in spray coating, the spreading behaviour is responsible for the deposition of the material. In this process, controlling the spreading will result in controlling the quality of the final product. In condensed mode polymerization, the contacting and evaporation of the liquid defines the efficiency of the cooling process, which ultimately controls the production capacity of the reactor. De Gennes, Rein and Bonn have published comprehensive reviews on the details of these phenomena [1–3].

Drop spreading on flat-plate geometries have been studied extensively in the past, experimentally [4–15] as well as theoretically [16–20]. Many of these studies focussed on the spreading behaviour of droplets impinging on solid surfaces, through simplification of this complex system by reducing the surface tension to viscosity ratio and/or reducing the impact velocity.

The impact velocity greatly influences the final equilibrium state of the droplet, these states have been classified in six regimes and are clearly explained by Rioboo et al. [15]. In this work, we will focus on the deposition regime with low droplet impact velocities. The spreading behaviour in the deposition regime has been classified in four separate regimes and detailed as well by Rioboo et al. [15].

A general relation for the temporal spreading width has been introduced by Tanner et al. [4], which was used for the complete wetting of silicone oil droplets on glass. The introduction of the power law $S \sim Ct^n$ to fit spreading data has been widely used to characterize spreading behaviour on a flat plate and associated contact angle dynamics in good agreement with experiments [10,18,21–23]. However in the condensed mode polymerization process and many other applications, droplets spread on particles, which can not be considered flat. The geometry of the substrate influences the spreading behaviour and in order to extend the knowledge to other geometries, we will study spherical substrates in this work.

To gain more information on the subject, two methods can be used to obtain information about the system. Experimental work allows for highly accurate data because the system studied provides the real world physics. However, certain aspects like detailed flow patterns are difficult to capture experimentally and therefore Computational Fluid Dynamics (CFD) provides a powerful tool to obtain such detailed information. In this study a fully resolved model will be used to study the droplet spreading process.

A lot of work has already been done and has mainly been focused on very specific aspects of droplet spreading on a spherical surface.

* Corresponding author.
E-mail address: m.w.baltussen@tue.nl (M.W. Baltussen).

https://doi.org/10.1016/j.powtec.2019.05.064

Iwamatsu used an energy balance approach to theoretically describe the equilibrium state of droplets on smooth spheres [24,25]. Pawar et al. looked into droplet-particle collision in free fall [26]. Bakshi et al. looked at the film-thickness of a droplet on a sphere [27]. Mitra et al. studied collision velocities, influence of heat transfer, particle deflection, film-thickness and spreading area [28–30]. Liu et al. studied symmetry breakage in collisions [31]. Eral et al. used electro wetting to study the effect of voltage on the contact angle [32]. Hardalupas et al. looked at droplet-particle collisions and the outcomes of these encounters [33]. Malgarinos et al. numerically studied the collisional regimes on spherical particles [34]. Banitabaei et al. studied experimentally and numerically the effects collision velocity and wettabillity on the collision outcome of a large droplet with a smaller particle. A comprehensive map is also presented with an overview of the work done based on impact velocity [35]. Liang et al. looked into the spreading behaviour on wetted spheres and varied the collisional velocity and curvature ratio [36]. Zhang et al. investigated numerically, with a lattice-Boltzmann model, the maximum spreading diameter, film-thickness and influence of curvature ratios [37]. Maheshwari et al. looked into the line tension and wettability of nano drops [38]. In this work, the focus lies in understanding the effect of the curvature on the spreading behaviour of a droplet. This behaviour is best studied by using a low velocity and a small Laplace number.

In order to obtain detailed information on the spreading behaviour of droplets on spherical substrates, fully resolved simulations based on an combined. Immersed Boundary (IB) and Volume of Fluid (VOF) method have been conducted. The motivation for this choice is that the implementation of the contact-line dynamics can be done with relative ease. In addition mass conservation is guaranteed in this model. In Table 1 an overview is presented of several numerical techniques for complex free surface computations together with their advantages and disadvantages.

In the next section, the numerical model will be explained followed by the details of the simulations and the data analysis. The analysis itself will focus on the effects of contact angle, curvature ratio and size on the spreading behaviour of a single droplet.

Table 1
Overview of available numerical techniques for multi-phase systems with advantages and disadvantages.

	Advantages	Disadvantages	References
Front Tracking & Immersed Boundary	- Direct interface tracking - Resolved particles	- No break-up and coalescence - Not mass conservative - No contact line implementation	Deen et al. [48] Baltussen et al. [62,63]
Level-set & Immersed Boundary	- Break-up and coalescence - Resolved particles - Contact line implemented	- Not mass conservative - Numerical coalescence	Ge and Fan [64] Suh and Son [65]
Volume of Fluid & Immersed Boundary	- Mass conservative - Break-up and coalescence - Contact line implemented - Resolved particle	- Numerical coalescence - Indirect tracking of the gas-liquid interface	Washino et al. [66] Jain et al. [67] Karagadde et al. [68] Sun and Sakai [69] Baltussen et al. [39,70] Patel et al. [47] Tang et al. [71]

2. Model description

2.1. Governing equations

The current method is based on the VOF-IB method presented by Baltussen et al. [39]. It is suitable for simulating three-phase systems and involving fluid and solid interfaces.

In this model it is assumed that the fluids are Newtonian and incompressible, where one set of mass and momentum conservation equations is used (one-fluid formulation):

$$\nabla \cdot \mathbf{u} = 0 \tag{1}$$

$$\rho \frac{\partial \mathbf{u}}{\partial t} + \rho \nabla \cdot (\mathbf{u}\mathbf{u}) = -\nabla p + \nabla \cdot \boldsymbol{\tau} + \rho \mathbf{g} + \mathbf{F}_\sigma \tag{2}$$

where $\boldsymbol{\tau} = \mu[\nabla \mathbf{u} + (\nabla \mathbf{u})^T]$ is the fluid stress tensor and $\mathbf{F}_\sigma$ is a volumetric source term to include the effects of surface tension (σ) acting on curved fluid interfaces. For the density ρ and viscosity μ, linear and harmonic averaging are used, respectively [40]. To compute $\mathbf{F}_\sigma$, the Contiunum Surface Tension (CSF) method of Brackbill et al. [41] is used as shown in Eq. (3), where density scaling is applied to reduce parasitic currents and improve the numerical stability for high density ratio systems. This scaling distributes the acceleration due to surface tension symmetrically over the interface, conserving the total surface tension force [42].

$$\mathbf{F}_\sigma = \frac{\rho}{\langle \rho \rangle} \sigma \kappa \hat{\mathbf{n}} \tag{3}$$

In the CSF method, κ is the curvature of the surface and $\hat{\mathbf{n}}$ is the interface normal vector. In order to capture the dynamics of the fluid-interface, a VOF method is used. In this method the two fluids are tracked with a color function F, which represents the local fluid phase fraction. The evolution of the interface is captured by advecting F with the local fluid velocity as given by Eq. (4).

$$\frac{\partial F}{\partial t} + \mathbf{u} \cdot \nabla F = 0 \tag{4}$$

To solve Eq. (4) a geometrical advection scheme based on Piecewise Linear Interface Calculation (PLIC) [43] is used. The integration of the hyperbolic F-advection equation, Eq. (4), is the crucial part of the VOF method and is based on a pseudo-Lagrangian geometric advection scheme, which minimizes numerical diffusion. This method provides a high degree of mass conservation and a detailed explanation can be found by Van Sint Annaland et al. [44].

For the curvature calculations, the normals of the interface are calculated with the smoothed phase fraction using the smoothing polynomial proposed by Deen et al. [45].

Application of the smoothing method close to the solid interface gives non-physical values for the phase fractions, which can be overcome by extending the *F*-field into the solid region using a method proposed by Sussman et al. [46]. The simulations reported in this paper use an extension up to 4 grid-cells into the solid region. More information on this procedure can be found in Patel et al. [47].

In order to represent the fluid-solid interaction, an implicit second-order accurate IBM is used to apply no-slip boundary conditions for fluid-solid interaction in the staggered Cartesian grid [48,49]. Here the cells are flagged according to the position of their centers: cells inside a solid body are flagged “solid-cells” and otherwise are flagged “fluid-cells”. The velocity values near the boundary are expressed using an uni-directional quadratic interpolation polynomial in order to incorporate the no-slip boundary at the solid surface. More details of the method can be found in Deen et al. and Das et al. [48,50].

Table 2
Simulation parameters.

Parameters	Value	Unit
ρ_l	804	kg.m^{-3}
μ_l	$3.4 \cdot 10^{-2}$	Pa s
ρ_g	1.2	kg m^{-3}
μ_g	$2.0 \cdot 10^{-5}$	Pa s
σ	$3.2 \cdot 10^{-2}$	N m^{-1}
Θ	90°, 60°, 30°	degrees
R_d	0.05, 0.5	mm
La	2.2, 22	(−)

In three-phase flows, the contact line dynamics define the behaviour of the system in terms of wetting and de-wetting phenomena. To couple the VOF and IBM, a contact angle is applied as a boundary condition of the triple contact line in the CSF model. The boundary condition is applied by modifying the fluid-interface normals at the contact line. The interest of this work lies in the lower Reynolds range and allows us to use a model developed by Voinov and Cox [51,52]. A thorough explanation of this method can be found in Patel et al. [47].

2.2. Numerical method

In order to solve the conservation Eq. (1), (2) the finite volume method on a staggered Cartesian grid is used. The diffusion term is calculated implicitly, except for the mixed derivatives. For the spacial discretization of the convection terms in the momentum equations, a second order flux delimited Barton-scheme is used, while a second order central differencing scheme is used for the spacial discretization of the diffusion term. The momentum equation is solved using a fractional step method for the pressure-velocity coupling. The first step involves the calculation of an intermediate velocity from the momentum equation excluding the pressure gradient. In the second step, the Poisson equation, Eq. (5), is solved to compute the pressure correction which finally is used to compute the advanced time level velocity, Eq. (6).

$$\nabla \cdot \left\{ \frac{\Delta t}{\rho} \nabla(\delta p) \right\} = \nabla \cdot \mathbf{u}^* \tag{5}$$

$$\mathbf{u}^{k+1} = \mathbf{u}^* - \frac{\Delta t}{\rho} \nabla(\delta p) \tag{6}$$

2.3. Verification and validation

The implementation of the IBM has thoroughly been verified and validated by Deen et al. [48,53] using existing data from literature. The VOF method was extensively verified and validated by Van Sint Annaland et al. and Baltussen et al. [44,54]. The coupling of the IBM and VOF was verified and validated by Patel et al. [47]. Because this study will use the same methods and code implementations, the model will not be verified and validated again.

3. Simulations and data analysis

In our simulations a droplet is deposited onto a spherical surface with a low velocity ($We = 1 \cdot 10^{-5}$) under the influence of gravity. The drop and particle are classified according to the ratio of their surface area, $F = R_d^2/R_p^2$. To reduce interface oscillations, the simulated liquid is squalene oil, which has been widely used in experimental studies on droplet spreading [5,18,21,47,55,56]. Table 2 shows the properties and details used in the simulations. The diameter of the droplet is either 0.1 or 1 with 50 computational cells per diameter, which was established on basis of a grid convergence study.

In Fig. 1a the simulated equilibrium spreading radius is compared with the analytical counterpart revealing very good agreement. There is an increased deviation for $\Theta = 30°$ at lower curvatures, which is due to the viscous spreading. These simulations were not continued as the focus in this work lies on the dynamics of the spreading behaviour. Fig. 1b shows a parity plot with an error margin of 5%, revealing that the simulated results are within this margin. The equilibrium spreading width for a droplet on a flat plate was predicted with an error of 0.01% for $\Theta = 90°$, 0.85% for $\Theta = 60°$ and 2.92% for $\Theta = 30°$. The increase in error for lower contact angles is due to the thickness of the spreading layer, which thins out for larger spreading areas. This results in a lower resolution in the film layer.

To facilitate efficient comparison of the results obtained from the extensive simulations, the non-dimensional time τ defined by Eq. (7) is introduced. A complete description and reasoning for this particular choice can be found in Appendix B.

$$\tau = \frac{t}{\sqrt{\frac{\rho R_d^3}{\sigma}}} \tag{7}$$

When spreading on a flat plate is considered, the equivalent spreading radius is calculated [18] or measured [11] but when a droplet is

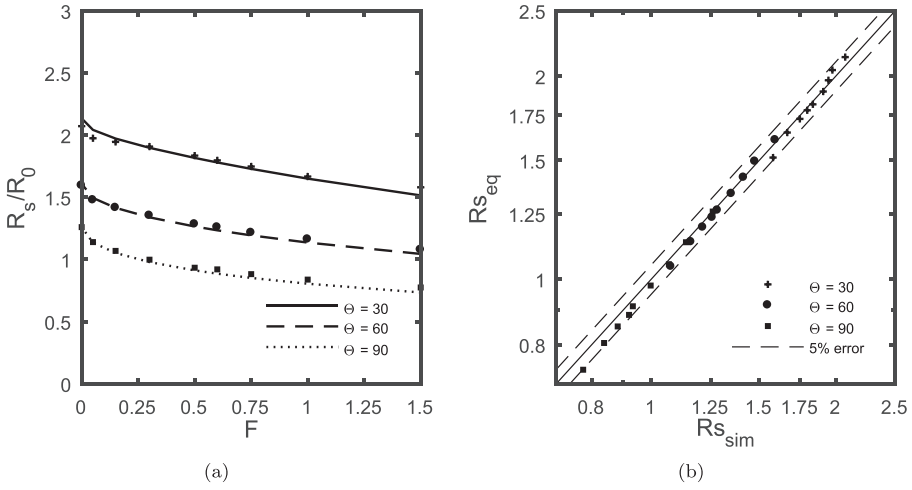

Fig. 1. a. Equilibrium spreading radius per curvature ratio for $\Theta = 30°$, 60° and 90°. The lines represent the analytical equilibrium values and the points represent the results from the simulations. b. Parity plot showing the spreading error margin between the simulation results and the theoretical values. The dashed lines represent the 5% error margin.

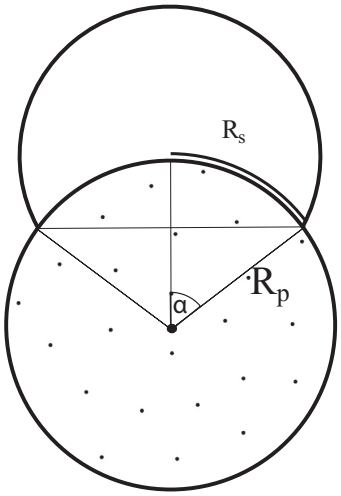

Fig. 2. Schematic representation of the spreading curvature estimation.

spreading over a sphere, the curvature is not always considered. As the spreading dynamics are dependent on the surface area of the substrate, the 2D equivalent spreading radius does not properly represent the geometry. Especially for droplets that spread over the equatorial plane of the spherical substrate, the spreading curvature is a better measure. This quantity can be estimated using the contact area, see Fig. 2, assuming that axi-symmetrical wetting prevails. To obtain the angle α, Eq. (8) is used, from which the dimensionless spreading curve is calculated using Eq. (9).

$$\alpha = \cos^{-1}\left(1-\frac{A_{wet}}{2\pi R_p^2}\right) \tag{8}$$

$$R_s = \frac{\alpha R_p}{R_0} \tag{9}$$

When Tanner introduced the power law as a tool to represent the spreading behaviour of droplets, the focus lied on the viscous spreading phase but the relation has also been used for the kinematic spreading and inertial spreading [4,57]. Legendre et al. considers the balancing of the capillary and inertial pressure to obtain Eq. (10) for the inertial-capillary spreading regime [18]. When scaling this equation with the non-dimensional time from Eq. (7), the pre-factor reduces to ~1 and results in Eq. (11).

$$R_s(t) \sim \left(\frac{\sigma R_0}{\rho}\right)^{1/4} t^{1/2} \tag{10}$$

$$R_s(\tau) \sim C\tau^n \tag{11}$$

Often, the focus lies on the exponent of the power law and is estimated by plotting the spreading radius on a logarithmic scale and fit the linear part with Eq. (11) [11,18]. The intricacy of fitting the pre-factor of the afore mentioned power law has been attempted as well but proved difficult due to interface oscillations [23,56]. In this work, the pre-factor C and the exponent n of Eq. (11) are fitted to the spreading radius (R_s) defined in Fig. 2.

4. Results and discussion

In Fig. 3, the time evolution of a spreading drop with $\Theta = 30°$ is shown. It shows the initial state, the kinematic spreading phase, the inertial spreading phase and the viscous spreading phase. The velocity inside the spreading drop is shown, revealing a complex flow pattern. When looking only at the shape of the droplet, these regimes are difficult to identify and often smoothly transition into one another.

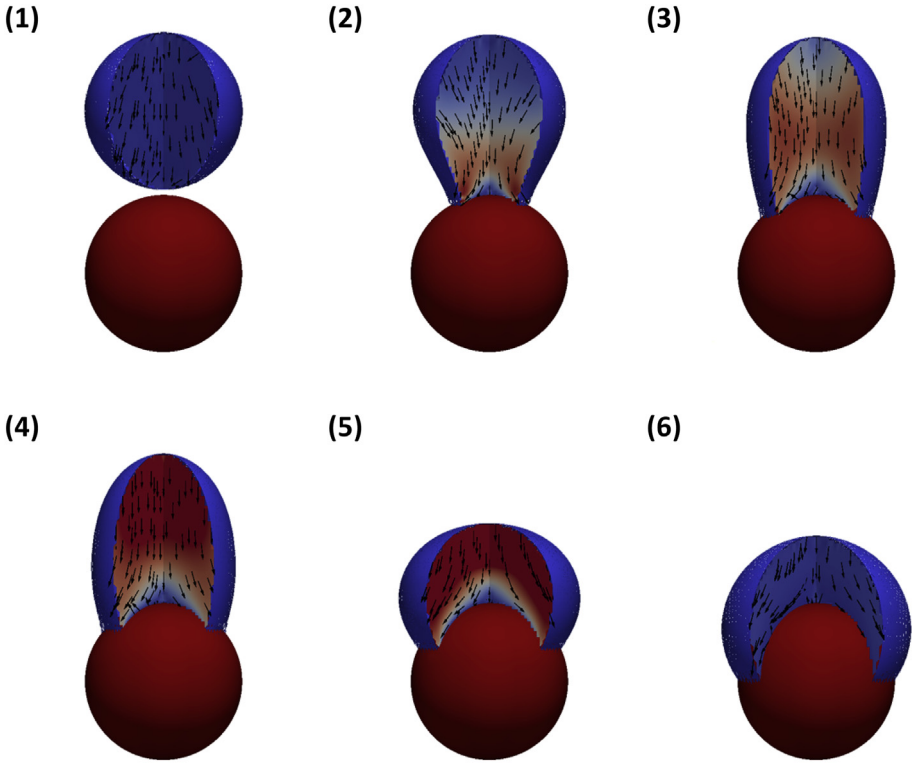

Fig. 3. Time evolution of a spreading drop with $\Theta = 30°$ and particle curvature F = 1.00. The first three images show the initial state and the kinematic spreading phase. The last three images show the inertial and the viscous spreading phase.

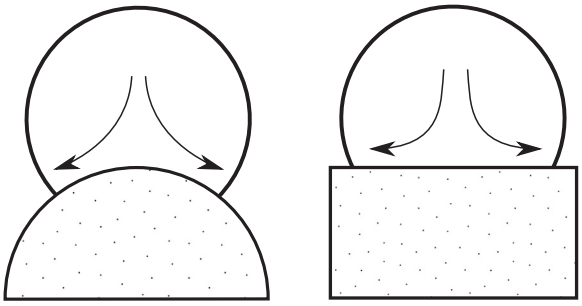

Fig. 4. Schematic representation of the change in direction of the initial momentum.

In the kinematic spreading phase, liquid needed for spreading is provided by the sides of the droplet. It starts to lose its spherical shape and becomes more elliptical. It can be noted that the height of the droplet remains almost unaffected. For the inertial phase, the surface tension pulls the bulk of the droplet towards the surface to provide more fluid for spreading. During this phase the height decreases significantly and almost reaches its final value. For higher contact angles $\Theta > 30°$, the fluid inertia often results in a maximum spreading diameter, which is generally larger than the equilibrium spreading diameter. After reaching its maximum the fluid retracts. For low contact angles, the next regime is the viscous spreading regime. This regime is governed by the viscous forces and its time scale is much larger than the time scale of the previous regimes combined.

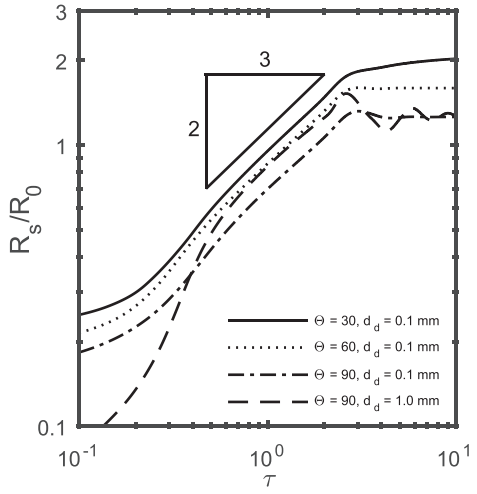

Fig. 6. Spreading rates for the flat-plate geometry. The exponent of the power law approximates $n \sim 2/3$ for the spreading of a low Laplace droplet.

The curvature of the surface affects the flowing patterns inside the droplet as schematically depicted in Fig. 4. With an increasing curvature

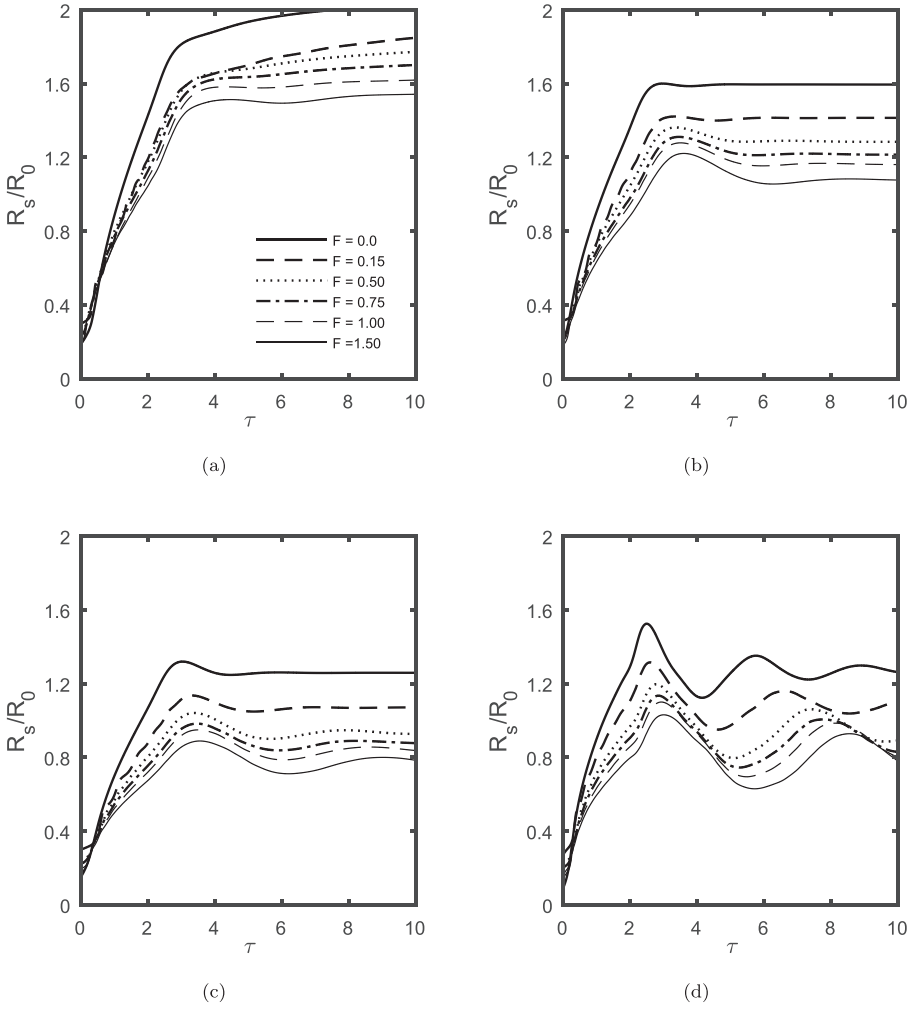

Fig. 5. Spreading behaviour for a droplet on multiple curvatures. 1.0 mm results in La = 22 and 0.1 mm results in La = 2.2 a. Droplet of size 0.1 mm with $\Theta = 30°$. b. Droplet of size 0.1 mm with $\Theta = 60°$. c. Droplet of size 0.1 mm with $\Theta = 90°$. d. Droplet of size 1.0 mm with $\Theta = 90°$.

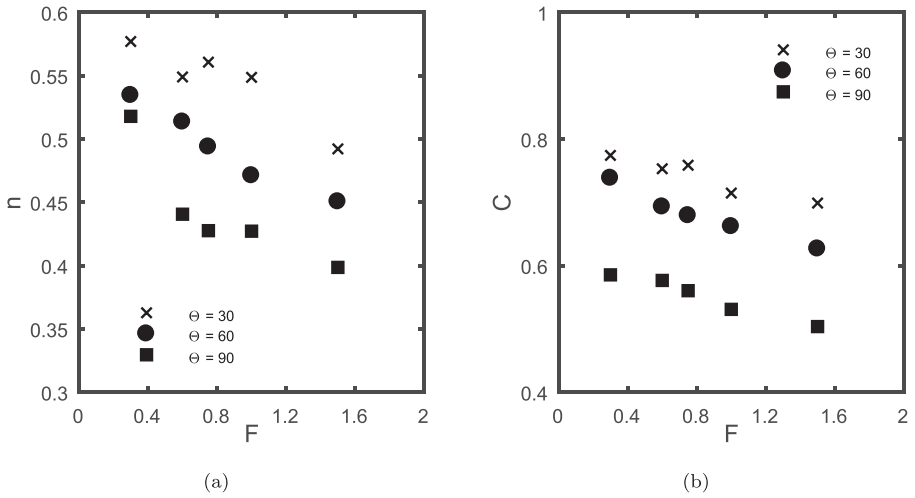

Fig. 7. Parameters of the power law fitted for Θ = 30°, 60° and 90° over the surface curvature F. a. Exponent *n*. b. Pre-factor F.

of the particle, the change in direction from the initial momentum is reduced. An increased angle of direction change also increases the momentum dissipation in the bulk of the droplet. Therefore, more oscillations are expected for surfaces with a higher curvature.

When examining the spreading data presented in Fig. 5, the increase in amplitude of the initial oscillation with decreasing particle size is indeed observed. This effect is more pronounced at higher contact angles and higher Laplace numbers. For the low contact angle Θ = 30° (Fig. 5a) the initial oscillation is smoothed out due to the increased spreading force. For less curved surfaces, the viscous spreading regime is more pronounced. An increase in curvature inhibits the viscous spreading phase, since more area has been covered by the initial spreading. For flat plate geometries the initial oscillations are quickly dampened out. For larger curvatures, the dampening takes more time as the initial amplitude is larger. Also, the energy dissipation in the bulk of the fluid is less pronounced due to the reduced equilibrium spreading radius for increased curvatures.

A less noticeable effect is the temporal displacement of the maximum spreading radius, i.e. it takes slightly more time to reach the maximum spreading radius when the curvature of the surface is increased. This is explained by the increased distance between the bulk and the contact-line. This combined with the reduced dissipation in the bulk results in the decrease of the oscillation frequency, which can be observed best in Fig. 5d.

One of the most obvious effects is the reduction in equilibrium spreading radius for increasing curvature. This is expected and can be predicted mathematically. The simulated equilibrium spreading radius matches within 5% error margin. Iwamatsu also predicted this with an energy balance approach [25].

Fitting the spreading data with the power law becomes increasingly challenging with the increase in curvature. This is due to the bend that appears around $\tau = 2.5$. Note that this behaviour is also visible for a flat-plate geometry for the larger Laplace number case in Fig. 5d.

This bend in the spreading radius indicates that the spreading behaviour is governed by at least two phenomena which have been identified as the kinematic and inertial regime. The kinematic regime is governed by the capillary forces at the contact line and the inertial regime is governed by the inertia of the bulk in motion. For a high Laplace number system with a small contact angle, the upper part of the droplet can be detached in the form of a satellite drop ejected from the roof of the parent drop, this effect has been observed by Ding et al. [58] and modelled by Das et al. [56].

For a flat-plate geometry, the kinematic regime seems to transition smoothly into the inertial regime. Fig. 6 shows the spreading radii for multiple contact angles and sizes, on a flat plate. Using the log scale on both axes, the initial spreading regime is visible as a straight line. The slope of this line represents the exponent of Eq. (11) and as shown in

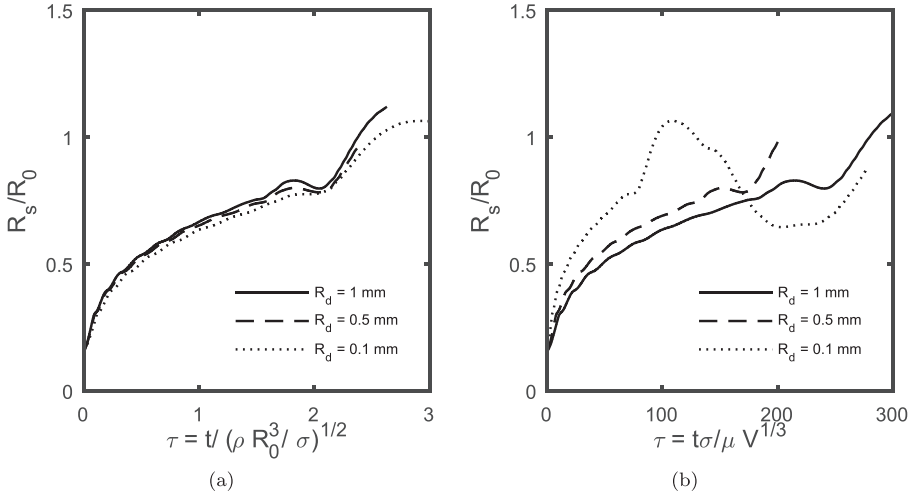

Fig. 8. Spreading radius for water droplets of three different sizes. a. scaled with $\tau = t/\sqrt{\rho R^3/\sigma}$. b. scaled with $\tau = t\sigma/\mu V^{1/3}$.

the figure, $n \approx 2/3$. This value has been reported for low Laplace number droplets in multiple publications [18,59,60].

For a surface with increased curvature, the separation between the two phenomena seems to be more pronounced. This complicates the fitting of the initial spreading curve and a choice has to be made which of the two phenomena should be considered in the fit. Due to the static contact angle approach taken in the model, the amplitude of the initial oscillation is over estimated as it should be partially compensated by the advancing contact angle. For this reason the kinematic spreading phase was chosen for the fitting of the power law to the spreading data.

In Fig. 7a and b the exponent and the pre-factor of the power law are plotted over F. The exponent n of the power law shows a linear decrease over the increase in curvature with a contact-angle dependence. This hints at a stronger deceleration of the contact line. Similar trends have been observed for increasing Laplace number by [18] and for increasing surface porosity by [56]. A linear decline is found for the pre-factor C, which shows a similar trend as the decrease in equilibrium spreading radius for increasing curvature. As expected there is a strong dependence on contact angle in the pre-factor.

5. Conclusions

The numerical results of this study show a change in spreading behaviour for spherical surfaces compared to flat surfaces. Through a systematic variation of curvature, its influence on different aspects of the spreading behaviour has been quantified through fully resolved simulations. At increased curvature, two spreading regimes exist during the initial spreading of low Laplace number droplets and consequently fitting with a single power law over the initial spreading phase becomes impossible.

Moreover, the spreading dynamics of the system changes when the curvature is increased, reducing the oscillation frequency, increasing the amplitude of the initial oscillation and reducing the damping of the oscillation.

When the power law is fitted over the kinematic spreading phase, a strong influence of curvature is seen in the exponent through a linear decline and a contact angle dependence. For the pre-exponent, the decrease is linear and strongly dependent on the contact angle as expected. The linear decline can be attributed to the reduction in equilibrium spreading radius for surfaces with a larger curvature.

Nomenclature

α	Surface wetted angle (degrees)
Θ	Contact angle (degrees)
κ	Curvature (m^{-1})
μ	Viscosity (Pa s)
ρ	Density ($kg\,m^{-3}$)
σ	Surface tension ($N\,m^{-1}$)
$\boldsymbol{\tau}$	Shear stress term ($N\,m^{-3}$)
τ	Dimensionless time (−)
A_{wet}	Droplet contact area (m^2)
C	power law pre-factor (−)
F	Phase fraction (−)
$\mathbf{F}_\sigma$	Surface tension source term ($N\,m^{-3}$)
g	Gravitational acceleration ($m\,s^{-2}$)
$\hat{\mathbf{n}}$	Surface normals(s)
n	power law exponent (−)
p	Pressure (Pa)
R_0	Initial droplet radius (m)
R_d	Droplet radius (m)
R_p	Particle radius (m)
R_s	Droplet spreading width (−)
S	Spreading diameter (−)
t	time (s)
$\mathbf{u}$	Velocity ($m\,s^{-1}$)
$\mathbf{u}^*$	Initial velocity estimation ($m\,s^{-1}$)
$La = \frac{\sigma\rho L}{\mu^2}$	Laplace number(−)
$We = \frac{\rho v^2 L}{\sigma}$	Weber number (−)

Acknowledgement

This work is part of the Research Programme of the Dutch Polymer Institute (DPI), PO Box 902, 5600 AX, Eindhoven, The Netherlands, project nr. #803.

Appendix A. Wet surface calculation

To be able to calculate the spreading area for each time-step, an algorithm was developed that estimates accurately the intersection area of the solid sphere through the grid-cell and multiplies the area times the phase fraction. This method works very well once the fluid has contacted the particle due to the extension of the phase-fraction into the solid surface. There is however a drawback, if the interface of the droplet is not contacting the solid surface but is present in the same grid-cell as the solid interface, this area will be considered and is added to the sum of the wetted area. This is incorrect and only occurs in the initial state before contacting the solid surface.

Appendix B. Time scaling comparison

In order to non-dimensionalise the time scale, multiple possibilities are available. Rioboo et al. uses the drop impact velocity and the initial diameter as $t^* = tv_{drop}/D_0$ for inertia driven impacts [15], some use the viscosity, surface tension and volume of the droplet $\tau = t\sigma/\mu V^{1/3}$ [1,4,6,8,12,61] and some use $\tau = t/\sqrt{\rho R_d^3/\sigma}$ which is the capillary inertial time [18,56]. This is an effort to be able to compare the impinging dynamics of systems with different fluid properties and dimensions.

In this work, two sizes of droplets are used. As can be seen in Fig. 8a and b, one scaling method is better at comparing droplets of different sizes. In this work the fluid viscosity, density and surface tension are not altered, there is no need to compensate for them in the time scaling. Furthermore the first scaling method has low values that seems to coincide with different aspects of the spreading behaviour, a more detailed analysis has been done by Das et al. [56].

References

[1] P. De Gennes, Wetting: statics and dynamics, Rev. Mod. Phys. 57 (3) (1985) 827.
[2] M. Rein, Phenomena of liquid drop impact on solid and liquid surfaces, Fluid. Dyn. Res. 12 (2) (1993) 61–93.
[3] D. Bonn, J. Eggers, J. Indekeu, J. Meunier, E. Rolley, Wetting and spreading, Rev. Mod. Phys. 81 (2) (2009) 739–805.
[4] L.H. Tanner, The spreading of silicone oil drops on horizontal surfaces, J. Phys. D 12 (9) (1979) 1473.
[5] M.D. Lelah, A. Marmur, Spreading kinetics of drops on glass, J. Colloid Interface Sci. 82 (2) (1981) 518–525.
[6] P. Ehrhard, Experiments on isothermal and non-isothermal spreading, J. Fluid Mech. 257 (1993) 463–483.
[7] J.A. Diez, R. Gratton, L.P. Thomas, B. Marino, Laplace pressure driven drop spreading, Phys. Fluids 6 (1) (1994) 24–33.
[8] F. Rieutord, O. Rayssac, H. Moriceau, Spreading dynamics of water droplets, Phys. Rev. E 62 (5) (2000) 6861.
[9] S.N. Reznik, A.L. Yarin, Spreading of a viscous drop due to gravity and capillarity on a horizontal or an inclined dry wall, Phys. Fluids 14 (1) (2002) 118–132.
[10] J.C. Bird, S. Mandre, H.A. Stone, Short-time dynamics of partial wetting, Phys. Rev. Lett. 100 (23) (2008), 234501.
[11] K.G. Winkels, J.H. Weijs, A. Eddi, J.H. Snoeijer, Initial spreading of low-viscosity drops on partially wetting surfaces, Phys. Rev. 5 (2012) 1–4.
[12] G.F. Teletzke, H. Ted Davis, L.E. Scriven, How liquids spread on solids, Chem. Eng. Commun. 55 (1–6) (1987) 41–82.
[13] Y. Yonemoto, T. Kunugi, Analytical consideration of liquid droplet impingement on solid surfaces, Sci. Rep. 7 (1) (2017) 2362.
[14] S. Chandra, C.T. Avedisian, On the collision of a droplet with a solid surface, Proc. R. Soc. A 432 (1884) (1991) 13–41.
[15] R. Rioboo, M. Marengo, C. Tropea, Time evolution of liquid drop impact onto solid, dry surfaces, Exp. Fluids 33 (1) (2002) 112–124.

[16] J. Fukai, Z. Zhao, D. Poulikakos, C.M. Megaridis, O. Miyatake, Modeling of the deformation of a liquid droplet impinging upon a flat surface, Phys. Fluids A 5 (11) (1993) 2588–2599.
[17] E. Ruckenstein, G.O. Berim, Microscopic description of a drop on a solid surface, Adv. Colloid Interf. Sci. 157 (1–2) (2010) 1–33.
[18] D. Legendre, M. Maglio, Numerical simulation of spreading drops, Colloids Surf. A Physicochem. Eng. Asp. 432 (2013) 29–37.
[19] I.V. Roisman, R. Rioboo, C. Tropea, Normal impact of a liquid drop on a dry surface: model for spreading and receding, Proc. R. Soc. A 458 (2022) (2002) 1411–1430.
[20] S. Wildeman, C.W. Visser, C. Sun, D. Lohse, On the spreading of impacting drops, J. Fluid Mech. 805 (2016) 636–655.
[21] B. Lavi, A. Marmur, The exponential power law: partial wetting kinetics and dynamic contact angles, Colloids Surf. A Physicochem. Eng. Asp. 250 (1–3) (2004) 409–414.
[22] L. Chen, E. Bonaccurso, M.E.R. Shanahan, Inertial to viscoelastic transition in early drop spreading on soft surfaces, Langmuir 29 (2013) 1893–1898.
[23] X. Frank, P. Perré, Droplet spreading on a porous surface: a lattice Boltzmann study, Phys. Fluids 24 (4) (2015), 042101.
[24] M. Iwamatsu, Line tension and morphology of a sessile droplet on a spherical substrate, Phys. Rev. E 93 (052804) (2016) 1–10.
[25] M. Iwamatsu, Spreading law on a completely wettable spherical substrate: the energy balance approach, Phys. Rev. E 95 (052802) (2017) 2–7.
[26] S.K. Pawar, F. Henrikson, G. Finotello, J.T. Padding, N.G. Deen, A. Jongsma, F. Innings, J.A.M. Kuipers, An experimental study of droplet-particle collisions, Powder Technol. 300 (2016) 157–163.
[27] S. Bakshi, I. V. Roisman, C. Tropea, Investigations on the impact of a drop onto a small spherical target, Phys. Fluids 19 (032102).
[28] S. Mitra, M.J. Sathe, E. Doroodchi, R. Utikar, M.K. Shah, V. Pareek, J.B. Joshi, G.M. Evans, Droplet impact dynamics on a spherical particle, Chem. Eng. Sci. 100 (2013) 105–119.
[29] S. Mitra, T.B.T. Nguyen, E. Doroodchi, V. Pareek, J.B. Joshi, G.M. Evans, On wetting characteristics of droplet on a spherical particle in film boiling regime, Chem. Eng. Sci. 149 (2016) 181–203.
[30] S. Mitra, G.M. Evans, E. Doroodchi, V. Pareek, J.B. Joshi, Interactions in droplet and particle system of near unity size ratio, Chem. Eng. Sci. 170 (2017) 154–175.
[31] Y. Liu, M. Andrew, J. Li, J.M. Yeomans, Z. Wang, Symmetry breaking in drop bouncing on curved surfaces, Nat. Commun. 6 (10034) (2015) 1–8.
[32] H.B. Eral, G. Manukyan, J.M. Oh, Wetting of a drop on a sphere, Langmuir 27 (9) (2011) 5340–5346.
[33] Y. Hardalupas, A.M.K.P. Taylor, J.H. Wilkins, Experimental investigation of submillimetre droplet impingement onto spherical surfaces, Int. J. Heat Fluid Flow 20 (5) (1999) 477–485.
[34] I. Malgarinos, N. Nikolopoulos, M. Gavaises, A numerical study on droplet-particle collision dynamics, Int. J. Heat Fluid Flow 61 (2016) 499–509.
[35] S.A. Banitabaei, A. Amirfazli, Droplet impact onto a solid sphere: effect of wettability and impact velocity, Phys. Fluids 29 (6) (2017), 062111.
[36] G. Liang, Y. Guo, X. Mu, S. Shen, Experimental investigation of a drop impacting on wetted spheres, Exp. Thermal Fluid Sci. 55 (2014) 150–157.
[37] D. Zhang, K. Papadikis, S. Gu, Investigations on the droplet impact onto a spherical surface with a high density ratio multi-relaxation time lattice-Boltzmann model, Communications in Computational Physics 16 (4) (2014) 892–912.
[38] S. Maheshwari, M. Van Der Hoef, D. Lohse, Line tension and wettability of nanodrops on curved surfaces, Langmuir 32 (1) (2016) 316–321.
[39] M.W. Baltussen, Q.I.E. Segers, J.A.M. Kuipers, N.G. Deen, Cutting bubbles with a single wire, Chem. Eng. Sci. 157 (2017) 138–146.
[40] A. Prosperetti, Navier-stokes numerical algorithms for free-surface flow computations: an overview, Drop-Surface Interactions, Springer 2002, pp. 237–257.
[41] J.U. Brackbill, D.B. Kothe, C. Zemach, A continuum method for modeling surface tension, J. Comput. Phys. 100 (2) (1992) 335–354.
[42] K. Yokoi, A density-scaled continuum surface force model within a balanced force formulation, J. Comput. Phys. 278 (2014) 221–228.
[43] D.L. Youngs, Time-dependent multi-material flow with large fluid distortion, Numer. Methods. Fluid Dyn. (1982).
[44] M. van Sint Annaland, N.G. Deen, J.A.M. Kuipers, Numerical simulation of gas bubbles behaviour using a three-dimensional volume of fluid method, Chem. Eng. Sci. 60 (2005) 2999–3011.
[45] N.G. Deen, M. van Sint Annaland, J.A.M. Kuipers, Multi-scale modeling of dispersed gas–liquid two-phase flow, Chem. Eng. Sci. 59 (8–9) (2004) 1853–1861.
[46] M. Sussman, An adaptive mesh algorithm for free surface flows in general geometries, Adapt. Method. Lines (2001) 207–231.
[47] H.V. Patel, S. Das, J.A.M. Kuipers, J.T. Padding, E.A.J.F. Peters, A coupled volume of fluid and immersed boundary method for simulating 3D multiphase flows with contact line dynamics in complex geometries, Chem. Eng. Sci. 166 (2017) 28–41.
[48] N.G. Deen, M. van Sint Annaland, J.A.M. Kuipers, Direct numerical simulation of complex multi-fluid flows using a combined front tracking and immersed boundary method, Chem. Eng. Sci. 64 (9) (2009) 2186–2201.
[49] S. Das, N.G. Deen, J.A.M. Kuipers, Direct numerical simulation for flow and heat transfer through random open-cell solid foams: development of an ibm based cfd model, Catal. Today 273 (2016) 140–150.
[50] S. Das, N.G. Deen, J.A.M. Kuipers, Immersed boundary method (ibm) based direct numerical simulation of open-cell solid foams: hydrodynamics, AICHE J. 63 (3) (2017) 1152–1173.
[51] O.V. Voinov, Hydrodynamics of wetting, Fluid Dyn. 11 (5) (1976) 714–721.
[52] R.G. Cox, The dynamics of the spreading of liquids on a solid surface. Part 1. Viscous flow, J. Fluid Mech. 168 (1986) 169–194.
[53] N.G. Deen, S.H.L. Kriebitzsch, M.A. van der Hoef, J.A.M. Kuipers, Direct numerical simulation of flow and heat transfer in dense fluid–particle systems, Chem. Eng. Sci. 81 (2012) 329–344.
[54] M.W. Baltussen, J.A.M. Kuipers, N.G. Deen, A critical comparison of surface tension models for the volume of fluid method, Chem. Eng. Sci. 109 (2014) 65–74.
[55] D. Legendre, M. Maglio, Computers & fluids comparison between numerical models for the simulation of moving contact lines, Comput. Fluids 113 (2015) 2–13.
[56] S. Das, H.V. Patel, E. Milacic, N.G. Deen, J.A.M. Kuipers, Droplet spreading and capillary imbibition in a porous medium: a coupled ib-vof method based numerical study, Phys. Fluids 30 (1) (2018), 012112.
[57] A.-L. Biance, C. Clanet, D. Quéré, First steps in the spreading of a liquid droplet, Phys. Rev. E 69 (016301) (2004) 1–4.
[58] H. Ding, E.Q. Li, F.H. Zhang, Y. Sui, P.D.M. Spelt, S.T. Thoroddsen, Propagation of capillary waves and ejection of small droplets in rapid droplet spreading, J. Fluid Mech. 697 (2012) 92–114.
[59] J. Drelich, D. Chibowska, Spreading kinetics of water drops on self-assembled monolayers of thiols: significance of inertial effects, Langmuir 21 (17) (2005) 7733–7738.
[60] L. Courbin, J.C. Bird, M. Reyssat, H. Stone, Dynamics of wetting: from inertial spreading to viscous imbibition, J. Phys. Condens. Matter 21 (464127) (2009) 13.
[61] O.V. Voinov, Wetting line dynamics in the process of drop spreading, J. Colloid Interface Sci. 226 (1) (2000) 22–28.
[62] M.W. Baltussen, L.J.H. Seelen, J.A.M. Kuipers, N.G. Deen, Direct numerical simulations of gas–liquid–solid three phase flows, Chem. Eng. Sci. 100 (2013) 293–299.
[63] M.W. Baltussen, J.A.M. Kuipers, N.G. Deen, Direct numerical simulation of effective drag in dense gas–liquid–solid three-phase flows, Chem. Eng. Sci. 158 (2017) 561–568.
[64] Y. Ge, L. Fan, 3-d direct numerical simulation of gas–liquid and gas–liquid–solid flow systems using the level-set and immersed-boundary methods, Adv. Chem. Eng. 31 (2006) 1–63.
[65] Y. Suh, G. Son, A sharp-interface level-set method for simulation of a piezoelectric inkjet process, Numer. Heat Transf. B 55 (4) (2009) 295–312.
[66] K. Washino, H.S. Tan, A.D. Salman, M.J. Hounslow, Direct numerical simulation of solid–liquid–gas three-phase flow: fluid–solid interaction, Powder Technol. 206 (1–2) (2011) 161–169.
[67] D. Jain, J.A.M. Kuipers, N.G. Deen, Numerical study of coalescence and breakup in a bubble column using a hybrid volume of fluid and discrete bubble model approach, Chem. Eng. Sci. 119 (2014) 134–146.
[68] S. Karagadde, A. Bhattacharya, G. Tomar, P. Dutta, A coupled vof–ibm–enthalpy approach for modeling motion and growth of equiaxed dendrites in a solidifying melt, J. Comput. Phys. 231 (10) (2012) 3987–4000.
[69] X. Sun, M. Sakai, Numerical simulation of two-phase flows in complex geometries by using the volume-of-fluid /immersed-boundary method, Chem. Eng. Sci. 139 (2016) 221–240.
[70] M.W. Baltussen, J.A.M. Kuipers, N.G. Deen, A numerical study of cutting bubbles with a wire mesh, Chem. Eng. Sci. 165 (2017) 25–32.
[71] Y. Tang, J.A.M. Kuipers, B. Buck, S. Heinrich, N.G. Deen, Interface-resolved simulations of normal collisions of spheres on a wet surface, AICHE J. 63 (11) (2017) 4774–4787.